This article has been accepted for publication in a future issue of this journal, but has not been fully edited. Content may change prior to final publication. Citation information: DOI 10.1109/TCPMT.2021.3116946, IEEE Transactions on Components, Packaging and Manufacturing Technology

Embedded Inductors using Composite Magnetic Materials for 12 V to 1 V Integrated Voltage Regulators

Claudio Alvarez*, Prahalad Murali*,Madhavan Swaminathan*, Oishi Yusuke†, Takashiro Junichi†, Nagatsuka Ryo‡, Naoki Watanabe‡
*Georgia Institute of Technology, 3D Systems Packaging Research Center
†Panasonic Corporation
‡Panasonic Industrial Devices Sales Company of America

***Abstract*—Substrate-embedded inductors enable the miniaturization of power modules and Integrated Voltage Regulators (IVRs) with higher power efficiencies and performance. However, embedded inductors for single-stage 12 V or 48 V to 1 V high-conversion-ratio IVRs present new performance challenges due to limitations in magnetic materials, limited space, high frequency, and low duty cycle. In this work, we analyze 7 embedded inductor designs fabricated with four metal-polymer composites magnetic materials. These inductors have inductances ranging from 20 nH to 500 nH, DC resistances between 14 mΩ and 40 mΩ, and saturation currents from 100 mA to over 5 A. Each inductor is characterized for its small-signal spectra with and without DC bias current and for its large signal response. With all these measurements, a relation between the small and large signal losses is made, showing that using the new R_{acx} metric they are related by a factor κ. The measurements show that, in the MHz range, the large signal losses can be over 4 times larger than the small-signal ones. These analyses allow us to understand the material properties and modeling new magnetic materials targeted for high-conversion-ratio IVRs with input voltages greater than 5 V.**

I. Introduction

Increased functionalities and computational capacity of today's electronic systems have resulted in the need for higher power density and miniaturized voltage regulator modules. Power Delivery Network (PDN) and Voltage Regulators (VR) play an integral role in High Performance Computing (HPC) platforms. Typical Central Processing Unit (CPU) and System-of-Chip (SoC) in servers and data centers are grouped in racks that are powered by rails of 48 V which are then down-converted to 0.6-1.2 V to supply the SoCs. As shown in [1], this down conversion is typically achieved by several down conversion stages including 48 V to 12 V, 12 V to 1.7 V, and finally 1.7 V to 1 V with overall PDN system efficiencies of 75% or less. New technologies, based on Silicon and Gallium-Nitride MOSFET, allows for 99% efficiency fix ratio conversion of 48 V to 12 V using resonant switched capacitors [2] and >90% efficiency for conversion of 12 V to 0.6-1.2 V using discrete on-board switched inductor buck converters. However, on-board voltage regulator modules need to operate at a few 100's of kHz to achieve high system efficiency, but limiting the regulation bandwidth required by the SoCs. With an SoC's operating voltage of 1 V, the current can be of the order of 100's of amperes requiring power planes with very low impedance and a large amount of package power connections, otherwise, the routing resistance will significantly affect the overall efficiency. As shown in [3], the regulation bandwidth and efficiency can be increased by using heterogeneous integration of single-stage high-conversion-ratio Integrated Voltage Regulators (IVR) mounted in the same SoC package, and as close as possible to the CPU, as shown in Figure 1. In [3] it is shown that when compared to an IVR with an input voltage of 1.8 V, an IVR with 5 V input voltage reduces the routing losses by over 7 times whereas the reduction in routing losses is over 40 times for an input voltage of 12 V

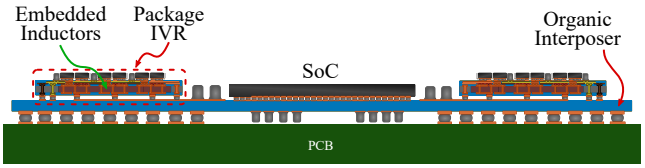

Fig. 1: Heterogeneous integration of package IVR.

IVRs require highly integrated components including power MOSFET and inductors. Embedding of passives components is key to obtain a smaller system size allowing them to be closer to the integrated circuits (IC), thus reducing the interconnection lengths and associated parasitics, and improving the power density. In particular, inductor embedding has been limiting the miniaturization and performance of IVRs [4]. This has been attributed to the limited performance of the commonly used magnetic materials such as ferrites and nanocomposite thin films with respect to the permeability, thickness, frequency stability, and loss properties of the materials. These factors affect the inductance and current density of the inductors. So far, an optimal trade-off between these performance parameters has been primarily achieved by surface-mount inductors. Novel inductor structures with high inductance density can make use of materials with lower permeability relaxing the constraints on saturation field and ferromagnetic resonance, according to Snoek's law.

To overcome the challenges of magnetic materials at high

2156-3950 (c) 2021 IEEE. Personal use is permitted, but republication/redistribution requires IEEE permission. See http://www.ieee.org/publications_standards/publications/rights/index.html for more information.
Authorized licensed use limited to: Georgia Institute of Technology. Downloaded on December 09,2021 at 23:19:42 UTC from IEEE Xplore. Restrictions apply.

This article has been accepted for publication in a future issue of this journal, but has not been fully edited. Content may change prior to final publication. Citation information: DOI 10.1109/TCPMT.2021.3116946, IEEE Transactions on Components, Packaging and Manufacturing Technology

frequency, IVRs have been using switching frequencies around 100 MHz, as shown in [5]–[12], where the required inductances is less than 10 nH. For high power SoC applications, air-core package embedded inductors were shown in [13] with implemented inductances in the range of 1 to 7 nH, with DC resistance in the range of 6 to 36 mΩ. Other magnetic thin-film technologies, as presented in [7], can achieve higher inductances close to 20 nH with high DC resistance of 92 mΩ. Even though these technologies can achieve very high inductance density, they cannot be scaled to obtain 100's of nH with DC resistances lower than 15 mΩ as required for single-stage high-conversion-ratio converters.

Recently, there has been a shift towards newer classes of materials such as metal-powders and metal-polymer composites (MPC) for inductors cores [14], [15]. In these materials, metal fillers coated with an insulating metal-oxide layer are embedded in epoxy polymers. The epoxy behaves as a distributed air gap reducing the core hysteresis losses and increasing the saturation magnetic field, while the small coated particle reduces the intra-particle eddy current losses. In [16] two magnetic composites material, Ni-Zn and CIP (cabonil-iron powder), were presented and compared using fabricated solenoid inductors. These materials use spherical fillers suporting over 8 A of saturation current, however, with a low relative permeability of less than 10. The inductors presented in [16] have an inductance of 24.5 nH and DC resistance of 22.4 mΩ using CIP, and inductance of 22.5 nH and DC resistance of 14.7 mΩ using Ni-Zn. In [17] a coaxial magnetic inductor was presented for the Integrated Voltage Regulators used on Intel CPUs, where vias are sorrounded by an MPC magnetic material with spherical fillers. These coaxial inductor shows an inductance of 2.5 nH up to 500 MHz with a DC resistance of 12 mΩ.

In this work, we leverage the advancement in composite magnetic materials, in the form of magnetic sheets, to fabricate several embedded inductors and characterize them. However in this work, the MPC materials are targeted for frequencies between 2 to 10 MHz and high relative permeability, as requried for high-conversion-ratio IVRs.

In this paper, we expand the work presented in [18] and [19]. Using a metal polymer composite (MPC) magnetic material with spherical fillers, in [18] we have presented a novel inductor power loss method and we have demonstrated it with small and large signal measurements. In [19] we have presented an array of embedded inductors using three different MPC magnetic materials with flake fillers, however, only the small signal measurments were performed. In this work, we have performed the small signal measurements with and without DC bias and the large signal measurements in a buck converter for all the inductors and materials presented previouly. We have completed the material analysis related to the work presented in [18] and the set of measurements for the work presented in [19]. This comprehensive set the fabrications and measurements cover a large range of results. These inductors have inductances ranging from 20 nH to 500 nH, DC resistances between 14 mΩ and 40 mΩ, and saturation currents from 100 mA to over 5 A, with measurements starting at 100 kHz up to 1 GHz. With these results we explore the capabilities of these materials and determine what are the material properties to make an inductor for 12 V and 48 V to 1 V IVR.

This work is structured as follows. Section II presents a review of the basic magnetic properties for metal-polymer composites. Section III shows the magnetic properties of the materials used in this work. Section IV shows the inductor models and fabrication results. Sections V and VI show the small signal spectra measurements with and without DC bias current, along with the r_{acx} metric. Section VII shows the large signal response and correlate the small and large signal losses. Finally, Section VIII shows a method to identify the possible conversion space (input to output voltage ratio) using a particular magnetic material, and determine what should be the magnetic properties required for a 12 V to 1 V IVR.

II. Review of Magnetic Properties for Composite Materials

As shown in [19], the required inductance for single-stage high-conversion-ratio IVRs ($V_{in} > 5$ V, $V_{out} = 1$ V) is in the order of 100's of nH with very low DC resistance of 15 mΩ and Effective AC Resistance per unit inductance R_{acx} less than 3 mΩ/nH. This last factor R_{acx} is a new metric introduced in [1] that allows to evaluate the small-signal inductor technology efficiency regardless of the amount of implemented inductance and inductor size. It considers the inductor current ripple harmonics as a function of frequency and duty cycle and is normalized to the inductance. This corresponds to an energy loss factor with units $1/s$ or Ω/H of the AC energy stored and transferred to the load. The inductor power loss P_L is related to the $R_{acx} = \kappa\, r_{acx}$ by (1)

$$P_L = I_L^2 R_{DC} + \Delta i_L^2 L(f_s)\kappa\, r_{acx}(D, f_s) \tag{1}$$

where κ is the small to large signal loss ratio (which is experimentally determined) and r_{acx} can be calculated by the next formula [1],

$$r_{acx} = \frac{2}{D^2(1-D)^2} \sum_{m=1}^{M} \frac{\sin^2(m\pi D)}{(m\pi)^4} \frac{R_{AC}(mf_s)}{L(f_s)} \tag{2}$$

where D is the buck converter duty cycle, R_{AC} and L are the small-signal AC resistance and inductance spectra, and f_s is the converter switching frequency.

For embedded inductors using a low-loss and high-permeability magnetic material as the core is imperative. Considering the drawback of ferrites and nanocomposite thin films as discussed earlier, the favorable class of materials for power inductors are the Metal-Polymer Composites (MPC). The permeability of particles in a MPC is different along different directions due to shape anisotropy [20]. If the magnetizing field $\vec{M}$ lies along with one of the principal axis of an ellipsoidal particle, the demagnetizing field $\vec{H}_M$ is given by $\vec{H}_M = -N\vec{M}$ with N being the demagnetizing factor. The value of N depends on the principal ellipsoid axis (a,b, or c) the field is directed to and it must obey the next relation,

$$N_a + N_b + N_c = 1$$

2156-3950 (c) 2021 IEEE. Personal use is permitted, but republication/redistribution requires IEEE permission. See http://www.ieee.org/publications_standards/publications/rights/index.html for more information.
Authorized licensed use limited to: Georgia Institute of Technology. Downloaded on December 09,2021 at 23:19:42 UTC from IEEE Xplore. Restrictions apply.

This article has been accepted for publication in a future issue of this journal, but has not been fully edited. Content may change prior to final publication. Citation information: DOI 10.1109/TCPMT.2021.3116946, IEEE Transactions on Components, Packaging and Manufacturing Technology

Three cases can be identified: Prolate spheroid (long rod), Oblate spheroid (disc or flake), and a Sphere. Figure 2 shows the values of N for the three cases. Depending on the inductor structure, composite fillers of one shape are preferable to others. It must be noted that the anisotropic shape factor does not depend on the specimen size.

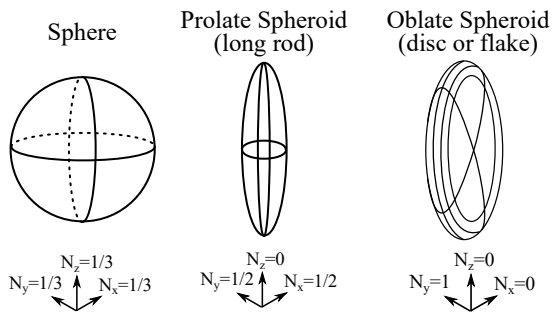

Fig. 2: Shape factor for different types of filler.

In a composite material, the effective permeability can be first approximated using [14],

$$\mu_e = 1 + \frac{p}{N_0(1-p) + 1/(\mu_i - 1)} \tag{3}$$

where p is the volume loading factor, N_0 is the demagnetization shape factor of magnetic fillers, and μ_i is the permeability of the magnetic fillers. Therefore, by increasing the loading factor and choosing the right filler shape the permeability can be increased. In MPC the effective relative permeability will be smaller than its bulk counterpart due to volume loading ratio and shape anisotropy [21].

The permeability spectra can be modeled using the Lorentz and Landau-Lifshitz-Gilbert equation shown in [14]. The equation is given by

$$\mu_e = 1 + \frac{\omega_d^2 \chi_{d0}}{\omega_d^2 - \omega^2 + j\beta\omega} + \frac{(\omega_s + j\alpha\omega)\omega_s \chi_{s0}}{(\omega_s + j\alpha\omega)^2 - \omega^2} \tag{4}$$

where χ_{d0} and χ_{s0} are the domain wall and spin magnetic susceptibilities, ω_d and ω_s are the resonant frequencies of each magnetic contribution, and α, β are damping factors. Since the permeability spectra is a complex value, it accounts for the inductance and the eddy currents losses in the magnetic material and windings. The core or hysteresis losses need to be calculated from the BH curve for the magnetic material. Therefore, a low coercivity is required for low hysteresis loss, and using a proper filler size in composite material is key because the size of the fillers has a direct impact on the coercivity $\vec{H}_c$ [22].

The ferromagnetic resonance limits the frequency stability of the inductor and is related to the shape factor, permeability, and magnetic saturation and there is a trade-off between permeability and ferromagnetic resonance where a high value for both cannot be obtained at the same time, this is called the Snoek's limit [15]. The FMR is defined by the Kittel expression shown in (5) [21].

$$f_{FMR} = \frac{\mu_0}{2\pi}\gamma\sqrt{[H_k + (A_x - A_z)M_s][H_k + (A_y - A_z)M_s]} \tag{5}$$

where M_s is the maximum attainable magnetization, H_k is the applied magnetic field, γ is the gyromagnetic ratio and is equal to 1.760859×10^{11} rad s^{-1} T^{-1}, and $\vec{A}$ is a demagnetizing factor that depends on the shape factor and volume loading fraction. For metal composite material with very low volume fraction $\vec{A} \approx \vec{N}$, and for a very high volume fraction (bulk limit) $\vec{A} \approx 0$.

For thin films or large magnetic sheets where large anisotropy is introduced, (5) is reduced to (6) [15],

$$f_{FMR} = \frac{\mu_0\gamma}{2\pi}\sqrt{H_k(H_k + M_s)} = \frac{\mu_0\gamma}{2\pi}\frac{M_s}{\mu_r - 1}\sqrt{\frac{H_k + M_s}{H_k}} \tag{6}$$

Reducing the particle size and volume loading ratio can also help to increase the FMR, since the polymer acts as a distributed air-gap which increases H_k. Regarding the eddy current losses, smaller particles exhibit lower induced current and therefore lower losses. However, when the volume loading is increased, particles start to touch each other increasing the effective particle size. To prevent this last issue particles can be coated with an oxide layer.

III. Magnetic Material Analysis

Three MPC materials HPE1, HPE2, and HBS1 were studied, along with RM4A [23] that is commercially available. These four materials are characterized for their permeability, loss tangent, resistivity, and magnetic saturation in order to analyze their efficiency for different IVR conversion ratios and frequencies. The permeability and loss tangent were measured using an impedance analyzer. Figure 3 shows the measured permeability for all four materials. The magnetization curve was measured using a vibrating sample magnetometer (VSM). Figure 4 shows the intrinsic magnetization B_i vs magnetic field intensity H, with $B = \mu_0 H + B_i$.

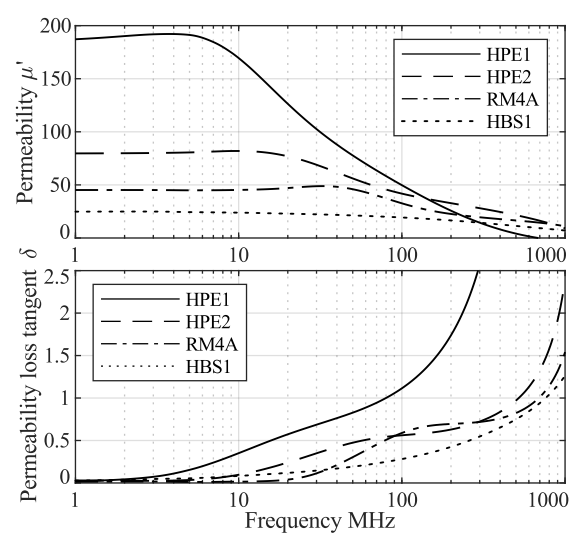

Fig. 3: Permeability Spectra of Magnetic Materials - HPE1, HPE2, HBS1 and RM4A.

From Figure 3, we observed that as the permeability decreases, the FMR increases (FMR is found close to where

2156-3950 (c) 2021 IEEE. Personal use is permitted, but republication/redistribution requires IEEE permission. See http://www.ieee.org/publications_standards/publications/rights/index.html for more information.
Authorized licensed use limited to: Georgia Institute of Technology. Downloaded on December 09,2021 at 23:19:42 UTC from IEEE Xplore. Restrictions apply.

This article has been accepted for publication in a future issue of this journal, but has not been fully edited. Content may change prior to final publication. Citation information: DOI 10.1109/TCPMT.2021.3116946, IEEE Transactions on Components, Packaging and Manufacturing Technology

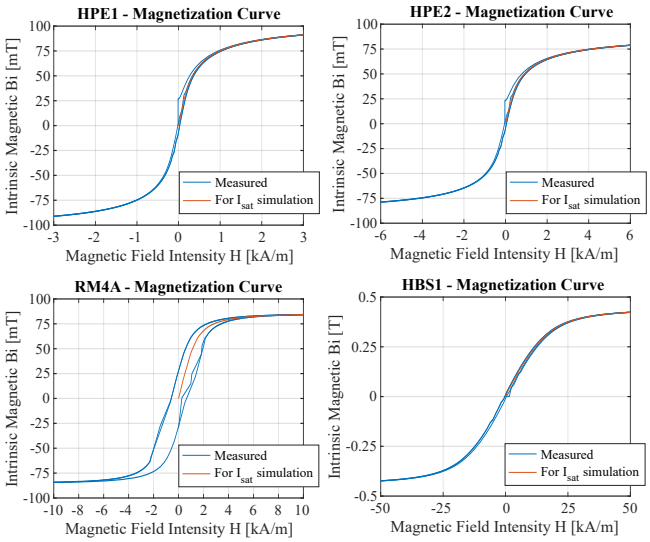

Fig. 4: B_i-H curves.

μ' start to decrease). From Figure 4, we can observe that as the permeability decreases the saturation field $\vec{H}_s$, where H start to flatten, increases. We can also see that three of the materials behave almost hysteresis-less. However, in the MHz regime, the hysteresis losses become important despite this observation.

IV. Inductor Fabrication Results

In this work, seven inductor designs were fabricated. These inductors were initially introduced in [24] and [19]. Figure 5 shows the top view of all the inductors along with their dimensions, and Figure 6 shows the fabrication results. Inductor IND034-IND037, IND046, and IND047 were fabricated on the same substrate (magnetic sheet), while IND048 was fabricated as an inductor array of 16 elements.

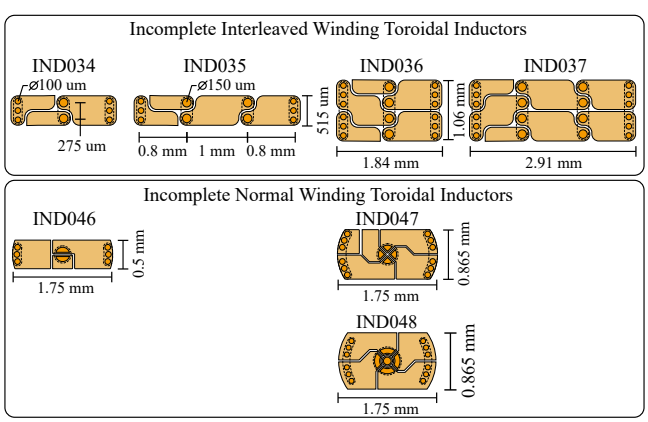

Fig. 5: Inductor models with their dimensions.

In the samples of Figure 6(a), the four vias at the center were drilled directly on the magnetic material making contact with the metallic fillers. This allows us to measure the resistance between the vias that are 1 mm apart. Table I shows the measured resistance. With the small-signal spectra measurements

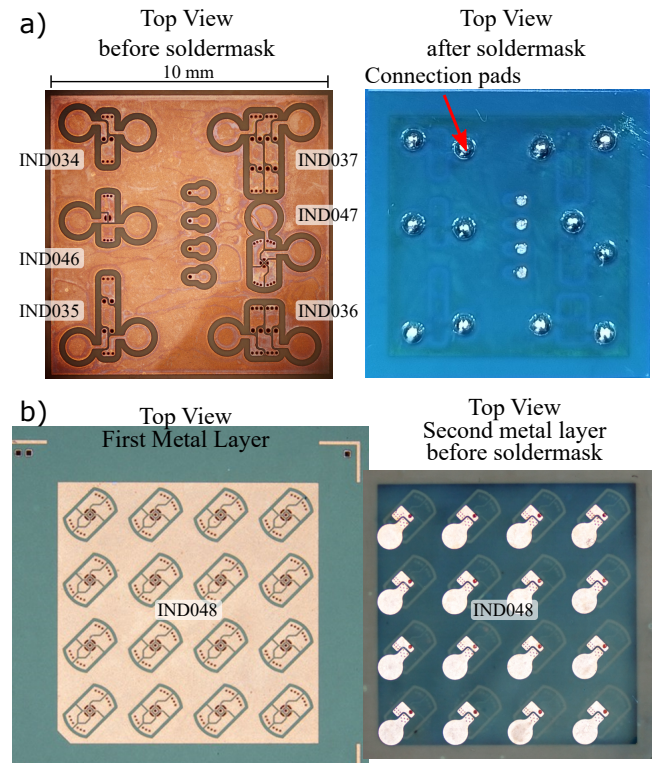

Fig. 6: Fabricated inductors.

TABLE I: Magnetic material resistance between 1 mm apart vias.

HPE1	HPE2	RM4A	HBS1
5.5 Ω	27 kΩ	50 MΩ	Hi-Z

and the r_{acx} metric, it will be clear the relation of high material conductivity and high small-signal losses.

The DC resistance was measured and averaged for all the inductors. Table II shows measured DC resistance. The simulated DC resistance was fitted to the measurements to estimate an electroplated copper conductance of 4.2 S/m.

TABLE II: Inductors DC resistance in mΩ with 25 μm electroplated copper thickness.

IND034	IND046	IND035	IND036	IND047	IND048	IND037
14.3	13.6	21.3	24.9	29.0	22.8	39.3

V. Small Signal Spectra

Figure 7 shows the small-signal inductance and resistance spectra of all the inductors. The figure shows in blue the measurements and in red the simulations. Both simulation and measurement, show excellent correlation.

With the extended frequency range from 100 kHz to 1 GHz it is possible to obtain the close-to-DC, AC, and RF responses. At 100 kHz we observe how the AC resistance converges to the DC resistance. We start to see a discrepancy at frequencies greater than 500 MHz for high inductance inductors, such as IND037, IND047, and IND048 with the low frequency materials and for inductor IND037 with material HBS1. This

2156-3950 (c) 2021 IEEE. Personal use is permitted, but republication/redistribution requires IEEE permission. See http://www.ieee.org/publications_standards/publications/rights/index.html for more information.
Authorized licensed use limited to: Georgia Institute of Technology. Downloaded on December 09,2021 at 23:19:42 UTC from IEEE Xplore. Restrictions apply.

This article has been accepted for publication in a future issue of this journal, but has not been fully edited. Content may change prior to final publication. Citation information: DOI 10.1109/TCPMT.2021.3116946, IEEE Transactions on Components, Packaging and Manufacturing Technology

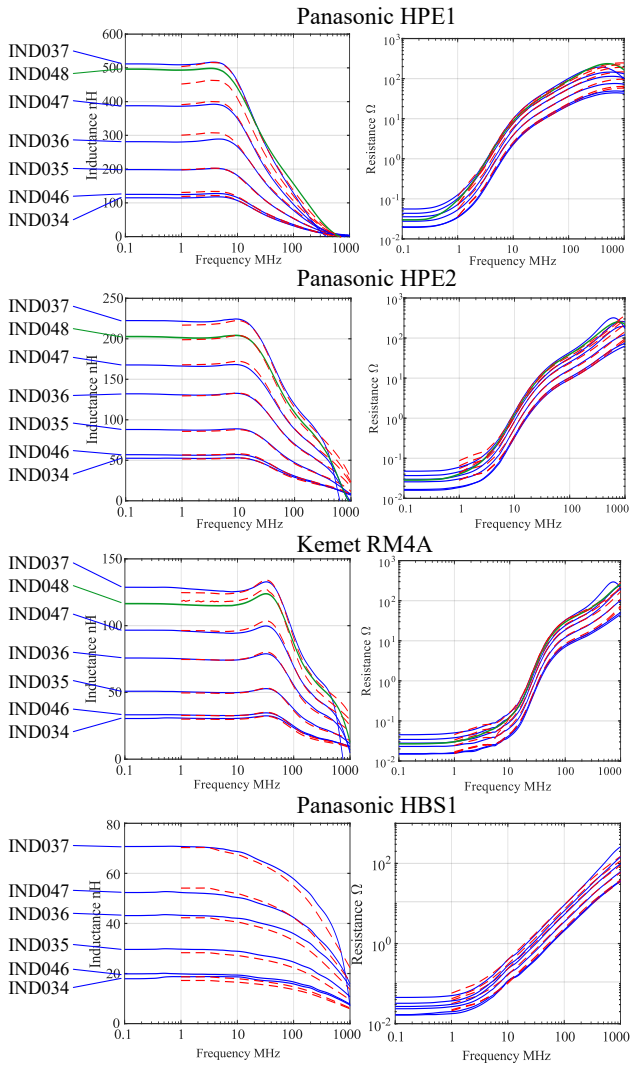

Fig. 7: Small signal spectra.

can be attributed to higher parasitic capacitances, however, it is not very relevant the inductor behavior above 500 MHz.

Using the measured spectra, we can use the expression (2) to compute the small-signal effective AC resistance per unit inductance r_{acx}. Figure 8 shows the extracted r_{acx}, material-wise. For each material, the r_{acx} is shown at different frequencies, and at each frequency each line corresponds to one of the inductor model shown in Figure 5. As it can be observed, this metric is not very sensitive to the amount of inductance or inductor structure, allowing its use, not only for power loss calculation but as a magnetic material performance metric.

The materials HPE1, HPE2, and RM4A have flake fillers. The r_{acx} of HPE1 is the larger as it is the one with the highest permeability, but also a higher bulk conductivity. The material HPE2 has a lower bulk conductivity showing lower losses. In the case of RM4A, it has no bulk conductivity and therefore the small-signal losses, due to eddy currents, are extremely low. The small signal performance of HBS1, which has spherical fillers, is comparable to HPE2 but with higher frequency stability.

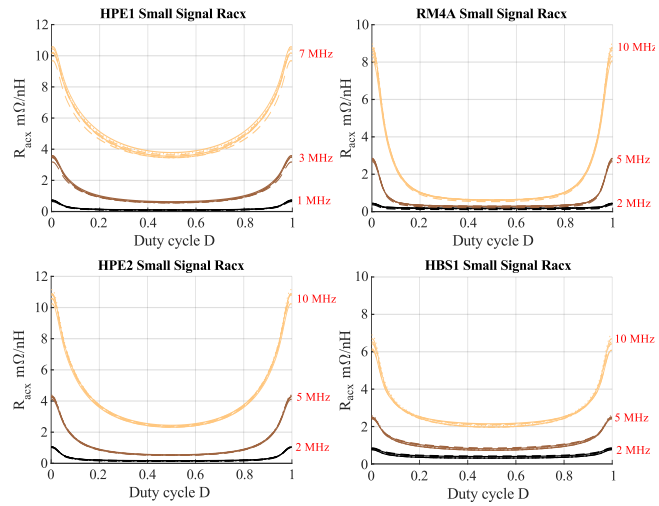

Fig. 8: Small signal r_{acx}.

From the r_{acx} curves, it can be observed that the resistance per unit inductance increases considerably with duty cycles below 20%. This shows how difficult it is to fabricate highly efficient inductors for high-conversion-ratio converter. In some 12 V to 1 V converter topologies the duty cycle can be around 19%, and in some 48 V to 1 V converter topologies the duty cycle can be less than 10%.

VI. Small Signal Spectra with DC Bias Current

Magnetic materials are highly non-linear with respect to both magnetic flux and frequency. By biasing the inductor with a DC current, the dependency of r_{acx} to the magnetic flux can be studied. Figure 9 shows the small-signal spectra with an applied DC bias current of some of the inductor structures. We observe that the low frequency materials start to saturate as soon as a small current of 100 mA is applied.

Figure 10 shows their inductance and r_{acx} variation as a function of the DC bias current. Since r_{acx} is a measure of the eddy current losses, in materials HPE1 and HPE2 the small-signal losses starts to decrease as the material becomes saturated as a consequence of a lower $d\phi(t)/dt$. In the case of RM4A, were the eddy current losses are already very small, the small-signal losses increase at higher currents. The low saturation point prevents any of these materials to be used in a buck converter, because only the inductor current ripple can be up to 500 mA. It is well known that air-gaps can increase the saturation current, but for embedded inductors, are required magnetic materials with engineered distributed air-gaps. The HBS1 material with spherical fillers have this property.

For material HBS1, the saturation current is above 5 A. The apparent increase of inductance is due to the error introduced by the current source's filter inductors that start to saturate at a current close to 5 A. We observe that at currents higher than 2 A, the DC resistance starts to increase due to Joule heating contributing to an increment in the r_{acx}. This material is fabricated using spherical fillers in a polymer matrix. As a result, between each spherical particle, there are small

2156-3950 (c) 2021 IEEE. Personal use is permitted, but republication/redistribution requires IEEE permission. See http://www.ieee.org/publications_standards/publications/rights/index.html for more information.
Authorized licensed use limited to: Georgia Institute of Technology. Downloaded on December 09,2021 at 23:19:42 UTC from IEEE Xplore. Restrictions apply.

This article has been accepted for publication in a future issue of this journal, but has not been fully edited. Content may change prior to final publication. Citation information: DOI 10.1109/TCPMT.2021.3116946, IEEE Transactions on Components, Packaging and Manufacturing Technology

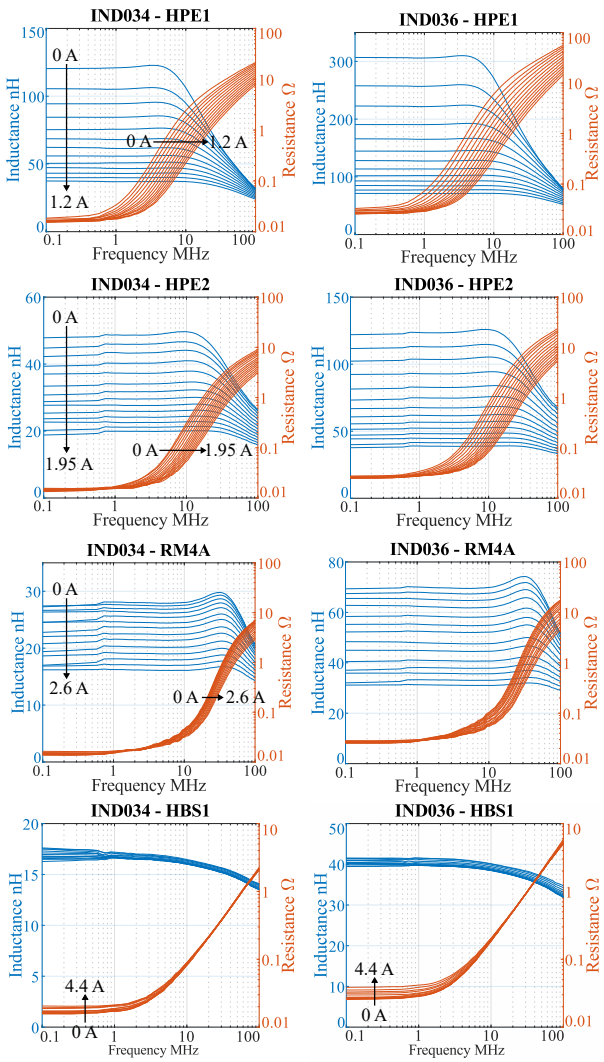

Fig. 9: Small signal spectra with DC bias current.

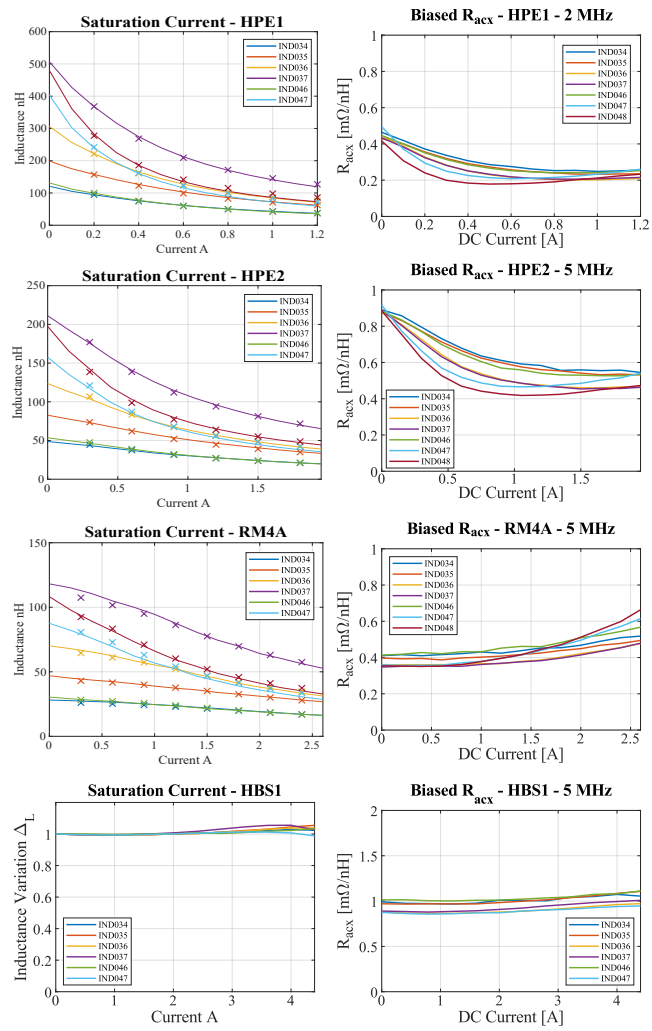

Fig. 10: Saturation current and small signal r_{acx} with DC bias current. Solid lines are from measurements, cross marks are from simulation.

gaps that act as distributed "air-gaps" decreasing the effective permeability and increasing the saturation current.

VII. Large Signal Response

To measure the large-signal AC response, the inductor is placed in a buck converter with no load (to force a zero DC current). The inductor voltage and current waveforms are obtained by a pair of 400 MHz bandwidth differential amplifiers. Figure 11 shows an example of recorded waveforms for the inductor voltage and current using an oscilloscope. The multiplication of these two gives the instantaneous power. Using the waveforms, the inductance is calculated as,

$$L = \frac{v_L \Delta t}{\Delta i} \tag{7}$$

and the current ripple is just the half peak-to-peak current. The inductor power loss is obtained with the average of the inductor power waveform.

$$P_L = \frac{1}{t_1 - t_0} \int_{t_0}^{t_1} v_L(t) i_L(t)\, dt \tag{8}$$

Finally, the measured large signal R_{acx} is simply,

$$R_{acx} = \frac{P_L}{\Delta i_L^2 L} \tag{9}$$

To study the large signal response, The inductors IND036 with HPE2 and IND037 with HBS1 were analyzed. Three different measurement sweeps were performed: current ripple, duty cycle, and frequency. These three measurements sweep allows us to determine up to what extent the κ factor, shown in the expression (1), remains constant or how it changes according to the parameter sweep. Figure 12 shows the recorded waveforms for the current ripple sweep for both inductors, and Tables III and IV show the extracted parameters.

For HPE2 we observe that, with as little as 80 mA, the extracted inductance is already different from what is expected due to saturation and losses with the average inductance being apparently larger (as the current increases, the hysteresis losses increases faster than the reduction of inductance due to saturation). With a saturated magnetic core, the relation between the small and large signal R_{acx} is not valid.

In the case of HBS1, the inductance values are correct over the entire current ripple sweep (the connection wires add

2156-3950 (c) 2021 IEEE. Personal use is permitted, but republication/redistribution requires IEEE permission. See http://www.ieee.org/publications_standards/publications/rights/index.html for more information.
Authorized licensed use limited to: Georgia Institute of Technology. Downloaded on December 09,2021 at 23:19:42 UTC from IEEE Xplore. Restrictions apply.

This article has been accepted for publication in a future issue of this journal, but has not been fully edited. Content may change prior to final publication. Citation information: DOI 10.1109/TCPMT.2021.3116946, IEEE Transactions on Components, Packaging and Manufacturing Technology

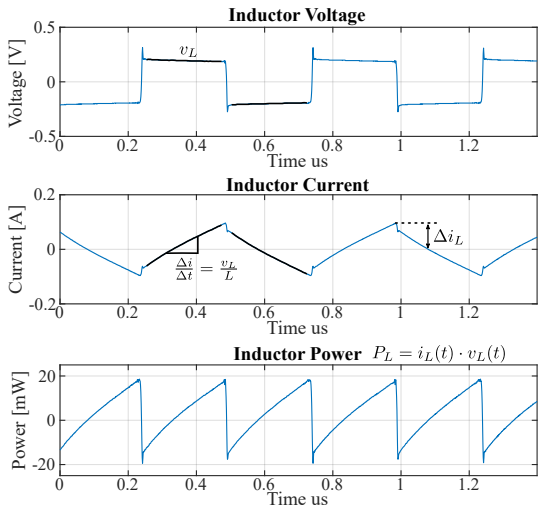

Fig. 11: Inductor waveform, parameter extraction.

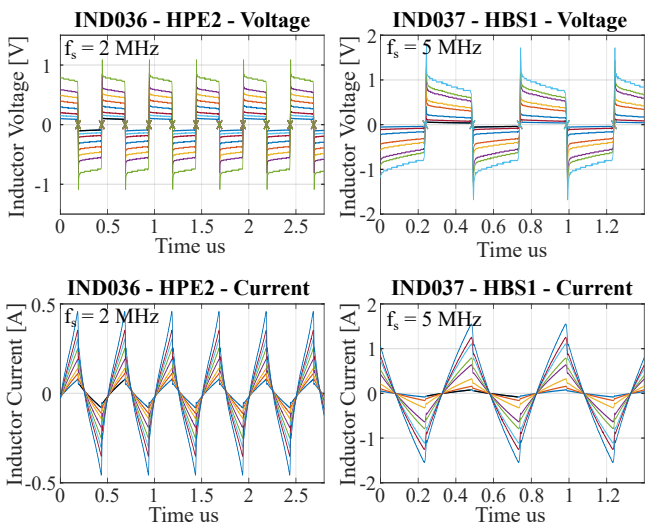

Fig. 12: Large-signal current ripple sweep.

around 10 nH of inductance). The large to small losses ratio κ is almost constant with an average value of 5.1 over a current ripple span of 600 mA. This seems to indicate that the small and large signal losses are related by a constant, at least in a narrow frequency band and with the magnetic core not close to saturation.

TABLE III: Inductor IND036 - HPE2 parameters from large-signal current ripple Δi_L sweep at $f_s = 2$ MHz. L_{sm} corresponds to the small-signal inductance.

L_{sm}	nH	130.4	130.4	130.4	130.4	130.4	130.4	130.4	130.4
r_{acx}	$\frac{\text{m}\Omega}{\text{nH}}$	0.146	0.146	0.146	0.146	0.146	0.146	0.146	0.146
L	nH	171.2	197.0	199.3	221.5	232.7	244.8	255.6	273.3
Δi_L	mA	81.30	111.8	140.2	191.1	250.0	302.8	351.6	457.3
P_{AC}	mW	1.312	3.024	5.513	12.59	23.66	37.30	53.85	96.86
R_{acx}	$\frac{\text{m}\Omega}{\text{nH}}$	1.160	1.294	1.406	1.558	1.626	1.661	1.704	1.694
κ	$\frac{R_{acx}}{r_{acx}}$	7.930	8.851	9.618	10.652	11.123	11.360	11.655	11.587

Figure 13 shows the recorded duty cycle sweep waveforms at a particular frequency for both inductors. For HPE2 the

TABLE IV: Inductor IND037 - HBS1 parameters from large-signal current ripple Δi_L sweep at $f_s = 5$ MHz. L_{sm} corresponds to the small-signal inductance.

L_{sm}	nH	69.8	69.8	69.8	69.8	69.8	69.8	69.8	69.8
r_{acx}	$\frac{\text{m}\Omega}{\text{nH}}$	0.753	0.753	0.753	0.753	0.753	0.753	0.753	0.753
L	nH	77.06	76.98	75.62	75.84	75.65	76.28	76.48	76.22
Δi_L	mA	77.24	149.4	227.6	300.8	373.9	447.2	513.2	584.4
P_{AC}	mW	1.656	6.609	14.95	26.55	41.63	59.87	80.09	105.2
R_{acx}	$\frac{\text{m}\Omega}{\text{nH}}$	3.602	3.847	3.814	3.869	3.934	3.925	3.976	4.043
κ	$\frac{R_{acx}}{r_{acx}}$	4.786	5.112	5.068	5.141	5.227	5.215	5.283	5.372

current ripple was limited to 40 mA to avoid saturation, and for HBS1 to 256 mA. The duty cycle sweep was recorded, for both materials, at frequencies 2, 3, 4, and 5 MHz. After extracting the large signal R_{acx}, the ratio κ was computed as shown in Table V. For frequencies above 4 MHz, in both materials the ratio κ seems to converge to a constant value.

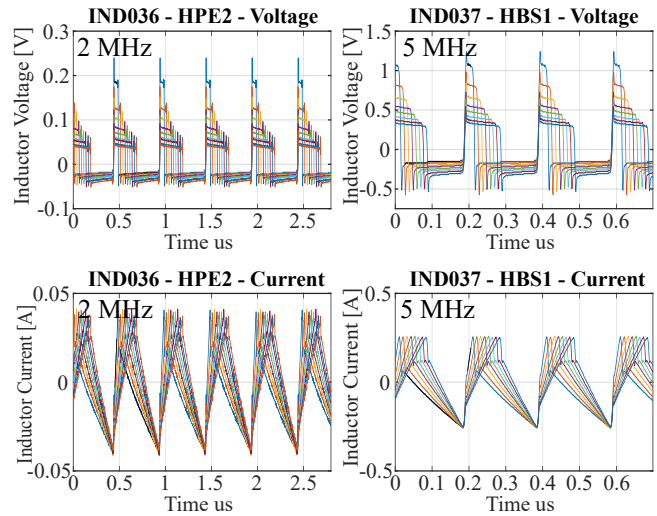

Fig. 13: Large-signal duty cycle sweep.

TABLE V: Large to small loss ratio κ as a function of frequency at $D = 0.5$.

f_s [MHz]		2	3	4	5
HPE2	κ	5.900	7.344	7.464	7.011
HBS1	κ	3.074	4.134	4.806	5.069

Using the ratios shown in Table V, Figures 14 and 15 show the relation between $\kappa\, r_{acx}$ (indicated by solid lines) and R_{acx} (indicated by the cross marks).

With HBS1, we observe that the large signal losses follow the same behavior of the small-signal ones. However, for HPE2 and frequencies above 4 MHz, the large signal losses do not follow the same trend at low duty cycles. We think this can be due to the proximity of the switching frequency f_s to the f_{FMR} of the material, which is around 10 MHz for HPE2.

From these measurements, we can expect the large-signal loss to be proportional to the small-signal loss by a factor κ,

$$R_{acx} = \kappa(f_s)\, r_{acx} \tag{10}$$

with κ constant with respect to the duty cycle and current ripple (provided the magnetic core not close to saturation, and

2156-3950 (c) 2021 IEEE. Personal use is permitted, but republication/redistribution requires IEEE permission. See http://www.ieee.org/publications_standards/publications/rights/index.html for more information.
Authorized licensed use limited to: Georgia Institute of Technology. Downloaded on December 09,2021 at 23:19:42 UTC from IEEE Xplore. Restrictions apply.

This article has been accepted for publication in a future issue of this journal, but has not been fully edited. Content may change prior to final publication. Citation information: DOI 10.1109/TCPMT.2021.3116946, IEEE Transactions on Components, Packaging and Manufacturing Technology

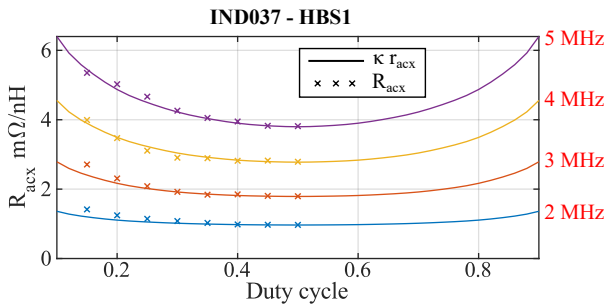

Fig. 14: Large signal R_{acx} of HBS1 material.

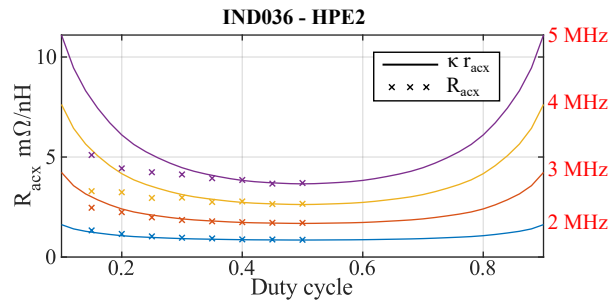

Fig. 15: Large signal R_{acx} of HPE2 material.

the switching frequency not close to the ferromagnetic resonance frequency of the material). With respect to frequency, it is needed to study it in a wider range to know its behavior at higher and lower frequencies. Asumming a constant value for κ in the frequency of interest $f_s > 2$ MHz, it can be possible to estimate the inductor power loss at some duty cycle D and switching frequency f_s with the next expression,

$$P_L = I_{DC}^2 R_{DC} + \Delta i_L^2 L \, \kappa \, r_{acx}(D, f_s) \tag{11}$$

VIII. Conversion Ratio Space

Using this comprehensive study of the four magnetic materials and the seven inductor designs, we are interested to know what are the capabilities of the materials. From the results, we see that only HBS1 can actually be used in power conversion applications, due to the need for a high saturation current. However, we need to know what are the possible conversion ratios where this material can be used, based on the inductor efficiency.

Using the AC power loss expression (1) and the expression for the current ripple $\Delta i_L = V(1-D)/2Lf_s$, we obtain

$$P_{L,AC} = \frac{V^2(1-D)^2}{4Lf_s^2} \kappa \, r_{acx}(D, f_s)$$

then, we can write the non-linear function $F(D)$ as follows,

$$F(D) = \frac{V^2(1-D)^2}{4Lf_s^2} \kappa \, r_{acx}(D, f_s) - P_{L,AC} = 0 \tag{12}$$

and solve for D for a given AC power loss $P_{L,AC}$. This will give us the allowed conversion ratios for a given inductor efficiency, where the inductor efficiency is given by,

$$\eta_L = \frac{I_L V}{P_{L,AC} + I_L^2 R_{DC} + I_L V} \tag{13}$$

For example, Figure 16 shows the conversion ratio space for material HBS1 considering an inductance of 65 nH (which could be obtained with IND048).

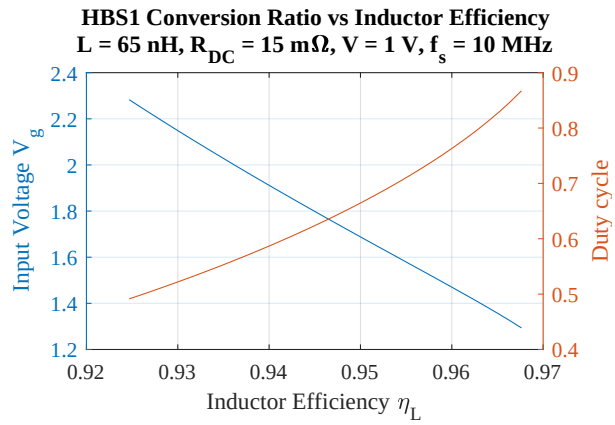

Fig. 16: Conversion space prediction for HBS1 material, using $\kappa = 5.1$

This inductor design framework, where the inductor properties are determined to satisfy a target inductor efficiency, allows to understand the limitations of the magnetic materials and inductor technology. Table VI shows the comparison of inductor model IND048 with material HBS1 to published embedded inductors with high inductance and low frequency. Based on inductor technology, we observed a higher L/R_{DC} ratio and a higher maximum current compared to other compact embedded inductors such as [26] and [27]. Thin-film inductors such as [28] can achieve very high inductance density but with very high DC resistance and very low current, limiting their application to low power devices. Non space-constrained inductors such as [25] and [29] can achieve a low DC resistance and high Q but at expense of inductance density, and therefore not suitable for IVRs.

We believe that combining our latest inductor model IND048 with a better magnetic material, the requirements for high voltage conversion ratio converter can be met. In the next section, we use the inductor design framework to determine the required magnetic properties.

IX. Magnetic Material Roadmap

Based on the analysed materials, the ideal material may need to have a combination of the properties of these two different magnetic composites. The low-frequency materials can achieve very low small-signal losses thanks to their flake fillers, creating a micro lamination structure. The ultra-low small-signal losses of RM4A indicate that the fillers must be coated with an insulating layer to prevent bulk conductivity. And, the distributed "air-gap" of the spherical fillers allows for a very high saturation current. We believe that a hybrid

2156-3950 (c) 2021 IEEE. Personal use is permitted, but republication/redistribution requires IEEE permission. See http://www.ieee.org/publications_standards/publications/rights/index.html for more information.
Authorized licensed use limited to: Georgia Institute of Technology. Downloaded on December 09,2021 at 23:19:42 UTC from IEEE Xplore. Restrictions apply.

This article has been accepted for publication in a future issue of this journal, but has not been fully edited. Content may change prior to final publication. Citation information: DOI 10.1109/TCPMT.2021.3116946, IEEE Transactions on Components, Packaging and Manufacturing Technology

TABLE VI: Comparison of properties of embedded inductor for integrated voltage regulators. † Small signal quality factor Q.

Property	This work HBS1-IND048	Spiral APEC 2018 [25]	Spiral APEC 2019 [26]	Toroid TPE 2019 [27]	Solenoid APEC 2020 [28]	Toroid CIPS 2020 [29]
Area	2.25×2.25 mm	15×15 mm	3.6×3.6 mm	2.4×2.4 mm	0.9 mm^2	10.5×10.5 mm
Thickness	600 μ	1.1 mm	288 μm	280 μm	<100 μm	500 μm
Material μ_r	24	180	–	3	800	34
Material Type	MPC	MPC	Fe composite	Ni-Zn composite	Thin-Film Co-Zr-Ta	Fe composite
Switching Frequency	10 MHz	2 MHz	16 MHz	12 MHz	10 MHz	2 MHz
Inductance L	60.7 nH	685 nH (L_{self})	150 nH	112 nH	75 nH	925 nH
Inductance Density	12.1 H/mm^2	3 nH/mm^2	11.5 nH/mm^2	19.4 nH/mm^2	83 nH/mm^2	8.4 nH/mm^2
DC Resistance R_{DC}	22.8 mΩ	40.7 mΩ	205 mΩ	265 mΩ	270 mΩ	66 mΩ
Maximum current	5 A	–	1 A	1.6 A	0.40 A	5 A
Current Density	1 A/mm^2	–	0.08 A/mm^2	0.270 A/mm^2	0.61 A/mm^2	0.05 A/mm^2
L/R_{DC}	2850 nH/mΩ	14574 nH/mΩ	731 nH/mΩ	422 nH/mΩ	277 nH/mΩ	14015 nH/mΩ
Peak $Q^\dagger$	15 (3.5 MHz)	–	38 (15 MHz)	14.3 (12.5 MHz)	14.5 (15 MHz)	28 (2 MHz)
Duty cycle D	60%	60%	66%	27%	28%	9.5%
r_{acx}	1.9 mΩ/nH	–	–	–	–	–
κ	5.1 (>5 MHz)	–	–	≈2.5 (12.5 MHz)	–	≈2.4 (2 MHz)

flake-spherical coated filler metal composite can be the key to achieve the required magnetic properties.

With the high inductance density of the inductor structure IND048, a material with relative permeability 45 can achieve 120 nH. Therefore, a material with a permeability of around 65 can achieve an inductance of 170 nH as required for 12 V to 1 V conversion ratio.

A theoretical material with the low loss characteristic of RM4A but with high enough saturation current, a large to small power loss ratio $\kappa = R_{acx}/r_{acx} = 4$, and an inductance of 170 nH, would give an inductor efficiency of 95% for 12 V to 1 V at 1.875 A, as shown in Figure 17. Note that in a two-phase series capacitor buck converter for 12 V to 1 V conversion [30], each phase is powered by 6 V, and Figure 17 shows 95% inductor efficiency with an input voltage of 6 V, or equivalently, a duty cycle of 0.19.

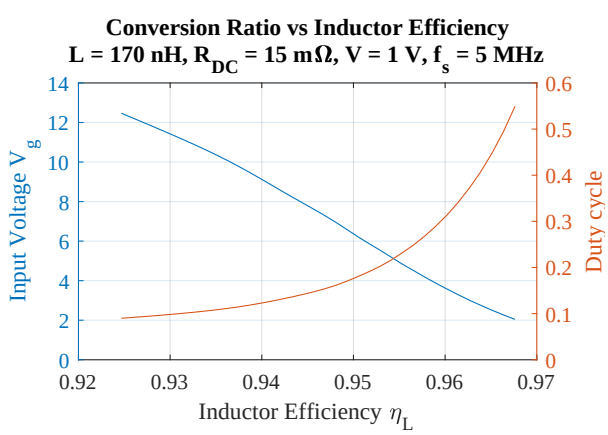

Fig. 17: Conversion space of the theoretical material required for 12 V to 1 V conversion at $f_s = 5$ MHz.

In Table VII it is summarized the key properties of the target magnetic materials to make 12 V to 1 V conversion IVRs possible.

X. Conclusions

In this work, we have presented the fabrication and measurement results for a large set of inductors. Seven inductor designs fabricated with 4 magnetic materials. These inductors have inductances ranging from 20 nH to 500 nH, DC resistances between 14 mΩ and 40 mΩ, and saturation currents from 100 mA to over 5 A. Three magnetic materials use flake fillers with high-permeability at low frequencies, and one material uses spherical fillers with low permeability stable up to higher frequencies.

TABLE VII: Key parameters for magnetic material for 12 V to 1 V conversion ratio IVR, at $f_s = 5$ MHz.

Parameters	Symbol	Units	Value
FMR	f_{FMR}	MHz	25
Switching Freq.	f_s	MHz	5
Permeability	μ'	-	65
Loss tangent	$\tan\delta$	-	0.012
Saturation	H_{sat}	kA/m	>6
Small Signal	r_{acx}	mΩ/nH	0.257
Loss ratio	κ	-	4

With the measured small-signal spectra with and without DC bias current, it was shown how the small-signal losses behave with respect to the different material, frequency, and bias current. It was observed that the materials with flake filler do not exhibit an effective distributed air-gap, this is reflected in a saturation current of less than 100 mA. In contrast, the HBS1 with spherical fillers can achieve saturation current over 5 A, but with lower inductance. It is well known that air-gaps can increase the saturation current, but for an embedded inductor, it is required a magnetic material with engineered distributed air-gaps like HBS1.

Using the large-signal measurements it was shown a relation between the large and small-signal losses. Using the new metric, it is shown that the relation $R_{acx} = \kappa(f_s)r_{acx}$ with κ constant with respect to duty cycle and current ripple is valid. This metric allows an easy evaluation of an inductor performance. It also allows us to determine the feasible voltage conversion ratio space for a particular magnetic material, and in a similar way, determine the required properties for a particular conversion ratio.

2156-3950 (c) 2021 IEEE. Personal use is permitted, but republication/redistribution requires IEEE permission. See http://www.ieee.org/publications_standards/publications/rights/index.html for more information.
Authorized licensed use limited to: Georgia Institute of Technology. Downloaded on December 09,2021 at 23:19:42 UTC from IEEE Xplore. Restrictions apply.

This article has been accepted for publication in a future issue of this journal, but has not been fully edited. Content may change prior to final publication. Citation information: DOI 10.1109/TCPMT.2021.3116946, IEEE Transactions on Components, Packaging and Manufacturing Technology

ACKNOWLEDGMENT

This work was supported in part by ASCENT, one of six centers in JUMP, a Semiconductor Research Corporation (SRC) program sponsored by DARPA. The authors wish to acknowledge the fabrication support provided by the Georgia Tech Packaging Research Center (PRC) consortium members for their support; The authors want to thank Dr. Jack Moon (GT-PRC) for help in material characterization; and Prof. Martin Mourigal (School of Physics, Georgia Institute of Technology) for VSM measurements.

REFERENCES

[1] C. Alvarez, S. Suresh, M. Swaminathan, R. Tummala, D. Sasaki, K. Watanabe, R. Nagatsuka, C. Ping Lin, T. Wada, and N. Watanabe, "Design and demonstration of single and coupled embedded toroidal inductors for 48v to 1v integrated voltage regulators," in *2020 IEEE 70th Electronic Components and Technology Conference (ECTC)*, 2020, pp. 405–413.

[2] Z. Ye, Y. Lei, and R. C. N. Pilawa-Podgurski, "A 48-to-12 v cascaded resonant switched-capacitor converter for data centers with 992500 w/in3 power density," in *2019 IEEE Applied Power Electronics Conference and Exposition (APEC)*, 2019, pp. 13–18.

[3] K. Radhakrishnan, M. Swaminathan, and B. K. Bhattacharyya, "Power delivery for high-performance microprocessors—challenges, solutions, and future trends," *IEEE Transactions on Components, Packaging and Manufacturing Technology*, vol. 11, no. 4, pp. 655–671, 2021.

[4] P. Raj, P. Chakraborti, D. Mishra, H. Sharma, S. Gandhi, S. Sitaraman, and R. M. Tummala, *Novel Nanostructured Passives for RF and Power Applications: Nanopackaging with Passive Components*, 2015.

[5] S. S. Kudva and R. Harjani, "Fully-integrated on-chip dc-dc converter with a 450x output range," *IEEE Journal of Solid-State Circuits*, vol. 46, no. 8, pp. 1940–1951, 2011.

[6] N. Sturcken, E. O'Sullivan, N. Wang, P. Herget, B. Webb, L. Romankiw, M. Petracca, R. Davies, R. Fontana, G. Decad, I. Kymissis, A. Peterchev, L. Carloni, W. Gallagher, and K. Shepard, "A 2.5d integrated voltage regulator using coupled-magnetic-core inductors on silicon interposer delivering 10.8a/mm2," in *2012 IEEE International Solid-State Circuits Conference*, Feb 2012, pp. 400–402.

[7] N. Sturcken, R. Davies, C. Cheng, W. E. Bailey, and K. L. Shepard, "Design of coupled power inductors with crossed anisotropy magnetic core for integrated power conversion," in *2012 Twenty-Seventh Annual IEEE Applied Power Electronics Conference and Exposition (APEC)*, 2012, pp. 417–423.

[8] C. Huang and P. K. T. Mok, "An 84.7% efficiency 100-mhz package bondwire-based fully integrated buck converter with precise dcm operation and enhanced light-load efficiency," *IEEE Journal of Solid-State Circuits*, vol. 48, no. 11, pp. 2595–2607, 2013.

[9] E. A. Burton, G. Schrom, F. Paillet, J. Douglas, W. J. Lambert, K. Radhakrishnan, and M. J. Hill, "Fivr — fully integrated voltage regulators on 4th generation intel core socs," in *2014 IEEE Applied Power Electronics Conference and Exposition - APEC 2014*, March 2014, pp. 432–439.

[10] K. Tien, N. Sturcken, N. Wang, J. Nah, B. Dang, E. O'Sullivan, P. Andry, M. Petracca, L. P. Carloni, W. Gallagher, and K. Shepard, "An 82%-efficient multiphase voltage-regulator 3d interposer with on-chip magnetic inductors," in *2015 Symposium on VLSI Circuits (VLSI Circuits)*, 2015, pp. C192–C193.

[11] C. . Chen, Y. . Hsu, J. . Hsieh, C. . Tsai, V. C. Y. Chang, A. Roth, E. Soenen, C. . Wang, and D. Yu, "Ultra-low-resistance 3d info inductors for integrated voltage regulator applications," in *2016 IEEE International Electron Devices Meeting (IEDM)*, 2016, pp. 35.2.1–35.2.4.

[12] M. Sankarasubramanian, K. Radhakrishnan, Y. Min, W. Lambert, M. J. Hill, A. Dani, R. Mesch, L. Wojewoda, J. Chavarria, and A. Augustine, "Magnetic inductor arrays for intel fully integrated voltage regulator (fivr) on 10th generation intel core socs," in *2020 IEEE 70th Electronic Components and Technology Conference (ECTC)*, 2020, pp. 399–404.

[13] W. J. Lambert, M. J. Hill, K. Radhakrishnan, L. Wojewoda, and A. E. Augustine, "Package inductors for intel fully integrated voltage regulators," *IEEE Transactions on Components, Packaging and Manufacturing Technology*, vol. 6, no. 1, pp. 3–11, 2016.

[14] M. L. F. Bellaredj, S. Mueller, A. K. Davis, Y. Mano, P. A. Kohl, and M. Swaminathan, "Fabrication, characterization and comparison of composite magnetic materials for high efficiency integrated voltage regulators with embedded magnetic core micro-inductors," *Journal of Physics D: Applied Physics*, vol. 50, no. 45, p. 455001, 2017.

[15] H. Song, "Soft magnetic composites for high frequency applications," in *Ph.D. dissertation in Oregon State University*, 2015.

[16] S. Müller, M. L. F. Bellaredj, A. K. Davis, P. A. Kohl, and M. Swaminathan, "Design exploration of package-embedded inductors for high-efficiency integrated voltage regulators," *IEEE Transactions on Components, Packaging and Manufacturing Technology*, vol. 9, no. 1, pp. 96–106, Jan 2019.

[17] K. Bharath, K. Radhakrishnan, M. J. Hill, P. Chatterjee, H. Hariri, S. Venkataraman, H. T. Do, L. Wojowoda, and S. Srinivasan, "Integrated voltage regulator efficiency improvement using coaxial magnetic composite core inductors," in *2021 IEEE 71th Electronic Components and Technology Conference (ECTC)*, 2021.

[18] C. Alvarez, P. Murali, M. Swaminathan, O. Yusuke, T. Junichi, N. Ryo, and N. Watanabe, "Proposed inductor power loss metric and novel embedded toroidal inductor for integrated voltage regulators," *IEEE Transactions on Components, Packaging and Manufacturing Technology*, 2021.

[19] C. Alvarez, P. Murali, M. Swaminathan, Y. Oishi, J. Takashiro, R. Nagatsuke, and N. Watanabe, "Demonstration of a high-inductance, high-density, and low dc resistance compact embedded toroidal inductor for ivr," in *2021 IEEE 71th Electronic Components and Technology Conference (ECTC)*, 2021.

[20] G. Bertotti, "Chapter 3 - maxwell's equations in magnetic media," in *Hysteresis in Magnetism*, ser. Electromagnetism, G. Bertotti, Ed. San Diego: Academic Press, 1998, pp. 73 – 102. [Online]. Available: http://www.sciencedirect.com/science/article/pii/B9780120932702500520

[21] R. Ramprasad, P. Zurcher, M. Petras, M. Miller, and P. Renaud, "Magnetic properties of metallic ferromagnetic nanoparticle composites," *Journal of Applied Physics*, vol. 96, no. 1, pp. 519–529, 2004.

[22] B. M. Moskowitz, "Hitchhiker's guide to magnetism," in *Environmental Magnetism Workshop*, 1991.

[23] K. a YAGEO Company, *Magnetic Sheet for RFID*, url: https://content.kemet.com/datasheets/KEM_FS8005_MSR.pdf.

[24] C. Alvarez, M. Bellaredj, and M. Swaminathan, "Open and closed loop inductors for high-efficiency system-on-package integrated voltage regulators," in *2019 IEEE 69th Electronic Components and Technology Conference (ECTC)*, May 2019, pp. 1672–1679.

[25] Y. Dou, Z. Ouyang, P. Thummala, and M. A. E. Andersen, "Pcb embedded inductor for high-frequency zvs sepic converter," in *2018 IEEE Applied Power Electronics Conference and Exposition (APEC)*, 2018, pp. 98–104.

[26] T. Fukuoka, Y. Karasawa, T. Akiyama, R. Oka, S. Ishida, T. Shirasawa, M. Sonehara, T. Sato, and K. Miyaji, "An 86% efficiency, 20mhz, 3d-integrated buck converter with magnetic core inductor embedded in interposer fabricated by epoxy/magnetic-filler composite build-up sheet," in *2019 IEEE Applied Power Electronics Conference and Exposition (APEC)*, 2019, pp. 1561–1566.

[27] H. T. Le, Y. Nour, Z. Pavlovic, C. O'Mathúna, A. Knott, F. Jensen, A. Han, S. Kulkarni, and Z. Ouyang, "High-q three-dimensional microfabricated magnetic-core toroidal inductors for power supplies in package," *IEEE Transactions on Power Electronics*, vol. 34, no. 1, pp. 74–85, 2019.

[28] S. L. Selvaraj, M. Haug, C. S. Cheng, D. Dinulovic, L. Peng, K. E. Shafey, Z. Ali, M. Shousha, Y. C. Ng, N. Aziz Yosokumoro, L. Lehmann, and M. Wieland, "On-chip thin film inductor for high frequency dc-dc power conversion applications," in *2020 IEEE Applied Power Electronics Conference and Exposition (APEC)*, 2020, pp. 176–180.

[29] R. Murphy, Z. Pavlovic, P. McCloskey, C. O Mathuna, S. O'Driscoll, and G. Weidinger, "Pcb embedded toroidal inductor for 2mhz point-of-load converter," in *CIPS 2020; 11th International Conference on Integrated Power Electronics Systems*, 2020, pp. 1–5.

[30] P. S. Shenoy, O. Lazaro, R. Ramani, M. Amaro, W. Wiktor, J. Khayat, and B. Lynch, "A 5 mhz, 12 v, 10 a, monolithically integrated two-phase series capacitor buck converter," in *2016 IEEE Applied Power Electronics Conference and Exposition (APEC)*, March 2016, pp. 66–72.

2156-3950 (c) 2021 IEEE. Personal use is permitted, but republication/redistribution requires IEEE permission. See http://www.ieee.org/publications_standards/publications/rights/index.html for more information.
Authorized licensed use limited to: Georgia Institute of Technology. Downloaded on December 09,2021 at 23:19:42 UTC from IEEE Xplore. Restrictions apply.

This article has been accepted for publication in a future issue of this journal, but has not been fully edited. Content may change prior to final publication. Citation information: DOI 10.1109/TCPMT.2021.3116946, IEEE Transactions on Components, Packaging and Manufacturing Technology

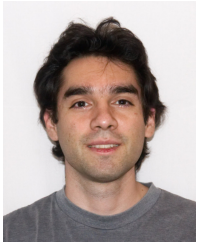

Claudio Alvarez Barros received his B.S. degree in electrical engineering from the Universidad de Santiago de Chile, in 2009. From 2010 to 2012, he worked in the international ALMA Radio Observatory. After that, he worked in other companies as an electronic and robotic engineer. In 2017 he was granted with a Fulbright fellowship from the US government and a CONICYT scholarship from the government of Chile to pursue a Ph.D. degree in the United States. He received the M.S. degree in 2019 and the Ph.D. degree in 2021. In Fall 2021 he joined Intel as Senior Analog Engineer.

Prahalad Murali received his B.Tech in Metallurgical and Materials Engineering from National Institute of Technology, Tiruchirappalli, India (NITT) in 2019. He is currently pursuing a Ph.D. degree in Materials Science and Engineering at the 3D Systems Packaging Research Center, Georgia Institute of Technology, Atlanta, GA, USA. He is advised by Prof. Madhavan Swaminathan and Prof. Mark Losego. His current research interests include fabrication of package embedded inductors and synthesis of magnetic materials for DC-DC converters.

Prof. Madhavan Swaminathan is the John Pippin Chair in Microsystems Packaging & Electromagnetics in the School of Electrical and Computer Engineering (ECE), Professor in ECE with a joint appointment in the School of Materials Science and Engineering (MSE), and Director of the 3D Systems Packaging Research Center (PRC), Georgia Tech (GT) (http://www.prc.gatech.edu). He also serves as the Site Director for the NSF Center for Advanced Electronics through Machine Learning (CAEML: https://publish.illinois.edu/advancedelectronics/) and Theme Leader for Heterogeneous Integration, at the SRC JUMP ASCENT Center (https://ascent.nd.edu/). Prior to joining GT, he was with IBM working on packaging for supercomputers. He is the author of 530+ refereed technical publications and holds 31 patents. He is the primary author and co-editor of 3 books and 5 book chapters, founder and co-founder of two start-up companies, and founder of the IEEE Conference on Electrical Design of Advanced Packaging and Systems (EDAPS), a premier conference sponsored by the IEEE Electronics Packaging Society (EPS). He is an IEEE Fellow and has served as the Distinguished Lecturer for the IEEE Electromagnetic Compatibility (EMC) society. He received his MS and PhD degrees in Electrical Engineering from Syracuse University in 1989 and 1991, respectively.

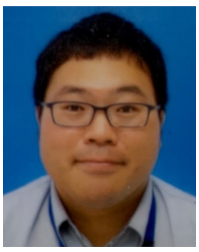

Oishi Yusuke is a staff engineer with Panasonic Electronic Materials Division. He earned a masters degree in biomolecular engineering from Kyoto Institute of Technology and has been with Panasonic Corporation since 2010. Over his career, Yusuke has conducted formulation design of epoxy molding compound for semiconductor packages including inductor.

Takashiro Junichi is an engineer with Panasonic Electronic Materials Division. He earned a masters degree in chemical engineering from Tokyo institute of technology and has been with Panasonic Corporation since 2013. Over his career, Junichi has conducted formulation design of sheet form epoxy molding compound for semiconductor packages including inductor.

Nagatsuka Ryo is an engineer with Panasonic Electronic Materials Division. He earned a masters degree in chemical bioengineering from Kansai University and has been with Panasonic Corporation since 2017. Over his career, Ryo has conducted formulation design of epoxy molding compound for semiconductor packages including inductor.

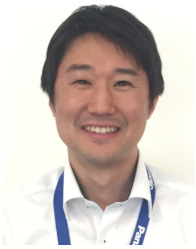

Naoki Watanable is a Senior Research Manager with Panasonic Electronic Materials Division. He earned a masters degree in chemical engineering from Kyoto University and has been with Panasonic Corporation since 2005. Over his career, Naoki has primarily conducted research on semiconductor packaging materials like epoxy molding compounds and capillary underfills. Most recently, he has been working in the United States developing advanced magnetic materials for embedded inductors. Naoki currently works in Mountain View, California and will return to Japan in 2022.

2156-3950 (c) 2021 IEEE. Personal use is permitted, but republication/redistribution requires IEEE permission. See http://www.ieee.org/publications_standards/publications/rights/index.html for more information.
Authorized licensed use limited to: Georgia Institute of Technology. Downloaded on December 09,2021 at 23:19:42 UTC from IEEE Xplore. Restrictions apply.